JOURNAL OF GUIDANCE, CONTROL, AND DYNAMICS
Vol. 32, No. 2, March–April 2009

Bifurcation and Stability Analysis of Aircraft Turning on the Ground

James Rankin*
University of Bristol, Bristol, England BS8 1TR, United Kingdom
Etienne Coetzee†
Airbus, Bristol, England BS99 7AR, United Kingdom
and
Bernd Krauskopf‡ and Mark Lowenberg§
University of Bristol, Bristol, England BS8 1TR, United Kingdom

DOI: 10.2514/1.37763

During ground maneuvers a loss of lateral stability due to the saturation of the main landing gear tires can cause the aircraft to enter a skid or a spin. The lateral stability is governed not only by aspects of the gear design, such as its geometry and tire characteristics, but also by operational parameters: for example, the weather and taxiway condition. In this paper, we develop an improved understanding and new presentation of the dynamics of an aircraft maneuvering on the ground, ultimately aimed at optimization and automation of ground operations. To investigate turning maneuvers, we apply techniques from dynamic systems theory to a modified version of a nonlinear computer model of an A320 passenger aircraft developed by the Landing Gear Group at Airbus in the United Kingdom. Specifically, we present a bifurcation analysis of the underlying solution structure that governs the dynamics of turning maneuvers with dependence on the steering angle and thrust level. Furthermore, a detailed study of the behavior when lateral stability is lost focuses on how the tire saturation at different wheel sets leads to qualitatively different types of overall behavior. The presented bifurcation diagrams identify parameter regions for which undesirable behavior is avoidable, and thus they form a foundation for defining the safe operating limits during turning maneuvers.

I. Introduction

THE dynamics of an aircraft's ground handling are governed by many different aspects of its design, loading, and operational practice. Factors such as the runway surface, weather conditions, and tire wear also play an important role. The handling qualities play a crucial part in safety and ride comfort. From a commercial point of view, the speed at which taxiing maneuvers are performed is important, because a reduction of time spent taxiing improves efficiency of operations at airports. Control of aircraft on the ground is one of the few areas in which automation has not been employed. The design of controllers to automate ground operations is heavily reliant on computer modeling and a greater understanding of ground maneuvers in general. In the past, computer modeling has been an invaluable tool in studying the ground dynamics of aircraft due to the high cost of real ground tests. Modeling and simulation have been used extensively in the design phases of new aircraft and for the analysis of existing aircraft (for example, to perform taxiway clearance tests). This paper focuses on an investigation into the stability of ground maneuvers in a medium-sized passenger aircraft. A computer model that includes important nonlinear effects is used to capture relevant behavior such as the lateral stability of the aircraft when cornering. Although simulations have been used previously to study ground maneuvers [1–3], nonlinear computer models have not been exploited to their full potential. Bifurcation analysis ([4], chapters 3 and 8, and [5], chapter 3) and continuation methods [6] (and [7], chapter 2) are powerful tools in the study of nonlinear dynamics. They have been used successfully alongside traditional analysis to investigate the dynamics of aircraft in flight [8], as well as the dynamics of vehicles on the ground [9], to identify regions of stability under the variation of system parameters. The introduction of these methods to the study of the nonlinear ground dynamics of aircraft is explained subsequently. First, the model used in our analysis is discussed.

When modeling a dynamic system it is important to identify, in as simple a model as possible, the significant components and appropriate levels of complexity to capture all relevant behavior. The model used here, designed with these considerations in mind, is a SimMechanics [10] model that was developed in parallel with a well-established ADAMS ([11], chapter 3) model of an Airbus A320 developed by the Landing Gear Group at Airbus, United Kingdom. The model was used for a previous investigation of nonlinear ground dynamics [12]. The software packages ADAMS and SimMechanics use a multibody-systems approach to study the dynamic behavior of connected rigid bodies that undergo translational and rotational displacements. Multibody-systems tools have previously been used to study aircraft models [13]. We consider a tricycle model on which the landing gears are connected to the airframe by translational joints (allowing displacement in the vertical axis only) for the main gears and a cylindrical joint (allowing displacement in, and rotation around, the vertical axis only) for the nose gear that steers the aircraft. The models for individual components and the forces acting on them and generated by them are constructed from test data, including nonlinear effects when appropriate. The main contributors to nonlinearity are forces on the tires, the oleo characteristics, and the aerodynamic forces generated by the airframe (see Fig. 1). The model was developed using data in normal operating regions of the aircraft with the aim that simulations be carried out within these regions. To study behavior outside of the normal operating regions (in particular, when lateral stability was lost), it was necessary to make some extensions to the parameter range of the model (see Sec. II).

We consider turning maneuvers that an aircraft may make when exiting the runway at high speed or taxiing to and from the airport terminal. Turns are made by adjusting the steering angle of the nose

Received 27 March 2008; revision received 12 May 2008; accepted for publication 12 May 2008. Copyright © 2008 by the American Institute of Aeronautics and Astronautics, Inc. All rights reserved. Copies of this paper may be made for personal or internal use, on condition that the copier pay the $10.00 per-copy fee to the Copyright Clearance Center, Inc., 222 Rosewood Drive, Danvers, MA 01923; include the code 0731-5090/09 $10.00 in correspondence with the CCC.

*Faculty of Engineering, Department of Engineering Mathematics.
†Systems Engineering Specialist, Landing Gear Systems.
‡Faculty of Engineering, Department of Engineering Mathematics.
§Faculty of Engineering, Department of Aerospace Engineering.

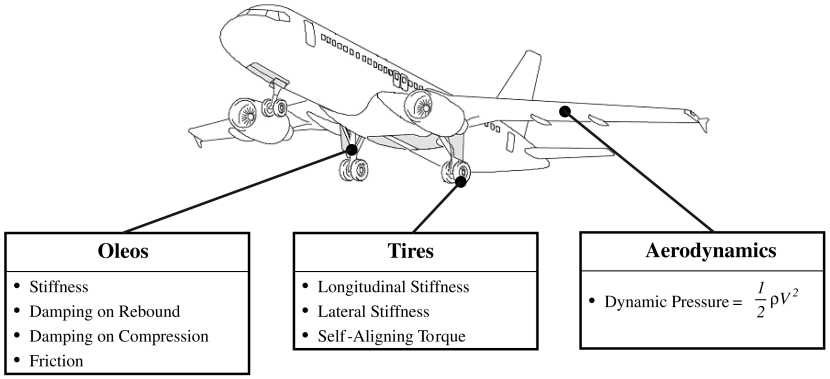

Fig. 1 Nonlinear components affecting aircraft ground dynamics.

gear while the aircraft is in motion. During ground operations the thrust may be changed occasionally to adjust speed, however, the thrust is kept constant during individual turns. We assume that no accelerations or braking forces are applied through the tires. In particular, we are concerned with turning maneuvers in which a fixed steering angle is applied for the duration of a turn; as an aircraft turns it follows a partial turning circle, and when the turn is complete the steering is straightened up. The performance of turning-circle maneuvers is a traditional test case for aircraft. Following a turning circle corresponds in the model to a steady-state solution for the aircraft because it does not undergo any accelerations in the body frame. In our analysis, we focus on fixed-steering-angle turning-circle solutions and their stability, because they dictate whether a particular turning maneuver is possible without a loss of lateral stability of the aircraft. We do not consider here any direct pilot or controller input, as are required for transient cases such as a lane-change maneuver. However, in the bifurcation analysis approach it would be possible to include pilot and/or controller action by considering an extended model.

Continuation is a numerical method used to compute and track or follow steady-state solutions of a dynamic system under the variation of parameters [14]. In our case, we treat the steering angle of the aircraft as a continuation parameter and hence compute how the turning-circle solutions change as the steering angle is varied. Although the thrust of the aircraft is kept constant for individual continuation runs, it is used as a second parameter, with continuation runs performed across a range of discrete thrust levels. Stability is monitored while solutions are being followed; changes in stability correspond to bifurcations, which are qualitative changes in the behavior of the system. Physically, changing the steering angle beyond a bifurcation point to a value for which the turning-circle solution is unstable can lead to a loss of lateral stability of the aircraft and therefore it can enter a skid or even a spin. One of the main strengths of the continuation methods used to produce this bifurcation analysis is the ability to identify safe parameter regions in which it is known that the aircraft will follow a stable turning circle. Additionally, it is possible to follow solutions when they are unstable, leading to the identification of physical phenomena that otherwise might not be detected with time-history simulations alone. The data produced from continuation can be represented in bifurcation diagrams of a parameter versus a state variable, which show how the solutions change by indicating stability and identifying bifurcation points. The bifurcation diagrams describe the underlying dynamic structure of a system from which we can explain the reasons for specific behavior (instead of just describing or observing it). This provides a more global picture of the dynamics of the nonlinear system: the aircraft during turning, in our case.

In this paper, we present a bifurcation analysis of a particular Airbus A320 configuration during turning maneuvers. Results were obtained by coupling the SimMechanics model with the continuation software AUTO [6] in MATLAB [10]. The use of continuation software facilitates the determination of the stability of turning operations, as described subsequently. We identify regions in the steering angle versus thrust parameter space for which the aircraft follows a stable turning circle or, if the turning-circle solution is unstable, a periodic motion. Note that although turning-circle solutions are spatially periodic, we do not consider them as periodic solutions here because the aircraft states remain constant in the body axis system. The bifurcation diagrams at two fixed-thrust levels for which the steering angle is varied are explained in detail, identifying the different kinds of solution and what it means to switch between these solutions. In the bifurcation diagrams, the solutions are shown in terms of the modulus of the velocity of the aircraft. To explain the dynamics represented by the diagrams, aircraft trajectory and time plots are used. The results for two parameters, the steering angle and the thrust level, are obtained by combining bifurcation diagrams over a range of discrete thrust levels. To summarize the behavior over the complete range of relevant values, a surface plot is rendered. The surface plot reveals robustness of the solution structure over the range of thrust levels. Therefore, by identifying regions of uniformly stable turning solutions in combination with information from the two fixed-thrust cases, the surface plot explains all relevant dynamics in a very compact way.

When lateral stability is lost, the aircraft performs a periodic motion relative to the now unstable turning circle. During the periodic motion the lateral stability of the aircraft is lost and it enters a skid or, in some cases, a spin before coming to a near or full stop. Because of the fixed thrust, the aircraft speeds up again before losing lateral stability once more, and therefore the motion is repeated periodically. Because of the way the model is implemented in SimMechanics it is not possible to use continuation to study these periodic solutions. Therefore, we use time-history simulations instead. Regions of qualitatively different behavior are identified along a branch of solutions. To explain the different types of periodic behavior, a new diagrammatic representation is introduced. For four qualitatively different cases, an ordered series of diagrams show how the state of the aircraft changes over one period of motion. Each series of diagrams describes the changes in the dynamic state of the aircraft in terms of its translational and rotational motion while identifying the saturation of individual tires. Together with the bifurcation analysis, our results give a full and detailed explanation of the stable dynamics of the aircraft over the entire range of relevant steering angle and thrust values.

The paper is organized as follows: In Sec. II, full details of the model are given. The results of the continuation analysis in the form of bifurcation diagrams and a global picture of the dynamics are given in Sec. III. In Sec. IV, periodic solutions are studied in detail. Finally, conclusions and directions of future work are presented in Sec. V.

II. Modeling of Aircraft and Components

The model of an Airbus A320 passenger aircraft that we study here is based on an ADAMS ([11], chapter 3) model. This model has been implemented in SimMechanics [10] so that it can be coupled with the continuation software AUTO [6] in MATLAB. ADAMS and SimMechanics are software packages using the multibody-systems approach to modeling dynamic behavior. Importantly, the package

Table 1 Aircraft dimensions

Length	37.6 m
Wingspan	34.1 m
Height	11.8 m
Fuselage width	4.0 m
Wheelbase	12.8 m
Track width	7.6 m

AUTO has direct control of the dynamic states in the SimMechanics model and therefore is using the system definition in an implicit way. Hence, we are able to study an industrially tested high-order model without the need for explicit equations.

We study a tricycle model in which the nose gear is used for steering. The model has 9 degrees of freedom (DOF): 6 DOF for the fuselage and 1 DOF for each of the oleos. Table 1 lists the dimensions of the aircraft. The lightweight case is considered here, in which there are no passengers or cargo and the minimal amount of fuel is onboard. The mass is 45,420 kg and we consider a forward position for the center of gravity (c.g.) (14% of the mean aerodynamic chord).

SimMechanics can analyze kinematic, quasi-static, and dynamic mechanical systems. The first step of the modeling is to describe the rigid parts and the joints connecting them ([11], chapter 3), in which a part is described by its mass, inertia, and orientation. The airframe is modeled as a rigid body to which the individual landing gears are connected. In the tricycle model considered here, the nose gear is constrained by a cylindrical joint and the main gears are constrained by translational joints. The next step is the addition of internal force elements, known as *line-of-sight* forces, to represent the shock absorbers and tire forces. External forces such as thrust and aerodynamic forces, known as *action-only* forces, are then added. All geometric aspects were parameterized, from the axle widths, wheel dimensions, gear positions, to the rake angles on the gears. This means that all joint definitions and forces are automatically updated when the design variables are changed. A schematic of the SimMechanics model is shown in Fig. 2.

Direct control of the steering angle is assumed, in that it is varied as a continuation parameter during the continuation runs. In all of the computations discussed next, the thrust is kept constant and a proportional–integral controller is used to find the desired thrust levels. Further details of the continuation process are explained in Sec. III.

Several nonlinear components are included in the model. The modeling of the tires, the oleos, and the aerodynamics is based on real test data. In each case, there are nonlinear relations depending on

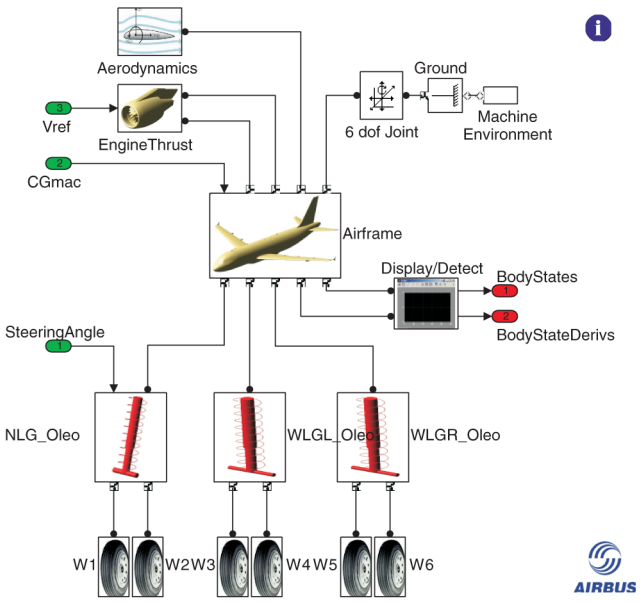

Fig. 2 SimMechanics representation of A320.

Table 2 Parameters values used to calculate the vertical tire force in Eq. (1)

Parameter	Description	Units	Nose	Main
m_t	Mass of tire	kg	21	75.5
k_z	Stiffness coeff.	kN/m	1190	2777
ζ	Damping ratio		0.1	0.1
c_z	Damping coeff.	Ns/m	1000	2886

dynamic states of the system. The data on which the models are based comes from tests performed within the normal operating regions for the aircraft. Previously, the model has been used by the Landing Gear Group at Airbus to generate results within these regions. To model the dynamics when the lateral stability of the aircraft is lost, it is necessary to study the behavior outside the normal operating regions. Therefore, it is required that the range of definition is extended in the models of certain components. The details of how this was done in the case of the tire model and aerodynamic forces is discussed now.

A. Tire Modeling

Apart from the aerodynamic, propulsive, and gravitational forces, all other loads on the aircraft are applied at the tire–ground interface. Tubeless radial tires are generally used for aircraft due to better failure characteristics when compared with bias-ply tires ([15], pages 8–18). In the model, there are two tires per gear, although due to the small separation distance, they can be assumed to act in unison; hence, they are described as a single tire in the rest of the paper. At lower velocities, the forces generated by the tires have a dominant effect over aerodynamic forces on the motion of the aircraft.

The vertical force component on the tire can be approximated by a linear spring and damper system ([11], chapter 4). The total force is

$$F_z = -k_z\delta_z - c_z V_z = -k_z\delta_z - 2\zeta\sqrt{m_t k_z}V_z \tag{1}$$

where V_z is the vertical velocity of the tire, and δ_z is the tire deflection representing the change in tire diameter between the loaded and unloaded condition. The coefficients are specified in Table 2.

Rolling resistance on hard surfaces is caused by hysteresis in the rubber of the tire. The pressure in the leading half of the contact patch is higher than in the trailing half; consequently, the resultant vertical force does not act through the middle of the wheel. A horizontal force in the opposite direction of the wheel movement is needed to maintain an equilibrium. This horizontal force is known as the *rolling resistance* ([15], pages 8–18). The ratio of the rolling resistance F_x to vertical load F_z on the tire is known as the *coefficient of rolling resistance* μ_R, where a value of 0.02 is typically used for aircraft tires [16]. We use an adapted Coulomb friction model:

$$F_x = -\mu_R F_z \tanh(V_x/\epsilon) \tag{2}$$

which incorporates a hyperbolic tangent function to approximate the switch in sign of the force when the direction of motion of the tire changes; the parameter ϵ governs the level of smoothing and is fixed to a value of $\epsilon = 0.01$.

When no lateral force is applied to a tire, the wheel moves in the same direction as the wheel plane. When a side force is applied to the wheel, it makes an angle with its direction of motion. This angle is known as the slip angle α, as depicted in Fig. 3a. For small slip angles, typically less than $\alpha = 5$ deg, the tire force increases linearly, after which there is a nonlinear relationship ([15], pages 30–38). The lateral force on the tire F_y is a function of α. It depends on the maximum lateral force $F_{y_{\max}}$ attainable by the tire at the optimal slip angle α_{opt}, as given by

$$F_y(\alpha) = 2\frac{F_{y_{\max}}\alpha_{\text{opt}}\alpha}{\alpha_{\text{opt}}^2 + \alpha^2} \tag{3}$$

The parameters $F_{y_{\max}}$ and α_{opt} depend quadratically on the vertical tire force F_z and hence change dynamically in the model. A function fitted to test data over the interval of $\alpha \in$ (0–40 deg) is plotted in

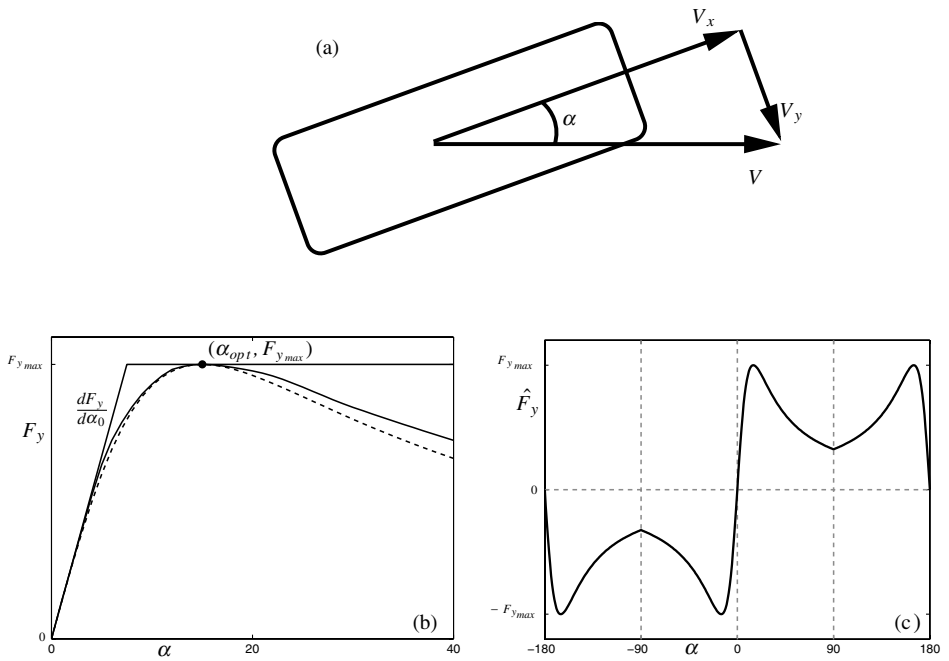

Fig. 3 Panel a shows how the slip angle α is calculated. Panel b shows how the normalized lateral tire force function, Eq. (3) (dashed curve), approximates test data for $\alpha \in$ (0–40 deg) (solid curve) for a given F_z. The function depends on the parameters $(\alpha_{opt}, F_{y_{max}})$ marked at the apex of the graph. The lateral tire stiffness is the gradient $dF_y/d\alpha_0$ of the curve at $\alpha = 0$. Panel c shows how the lateral force function is extended over the range of $\alpha \in (-180$–180 deg).

Fig. 3b as a solid curve. The lateral tire force F_y from Eq. (3) for the same F_z is plotted against tire slip angle α as a dashed curve. The tire stiffness $dF_y/d\alpha_0$ is the gradient of the function at $\alpha = 0$.

The lateral tire force function $F_y(\alpha)$ is fitted to test data for a nominal load F_z obtained in the normal region of operation of the aircraft [$\alpha \in$ (0–40 deg)]. In the original model, impulses on the force function are observed (at discontinuities at $\alpha = \pm 180$ deg) when operating outside this region. To study behavior outside of the normal operating region, it is necessary to extend the definition of the force function. First, with a change in sign of α, there is a corresponding change in the sign of F_y. To extend the range outside of $\alpha = \pm 40$ deg, we assume here that as the slip angle increases beyond $|\alpha| = 40$ deg, the force will continue to drop off because the size of the contact patch of the tire will continue to decrease when the slip angle increases. Furthermore, due to symmetry of the forces on the tire when it is rolling backward, it is possible to extend the definition of the function over the range of $\alpha \in (-180$–180 deg), with continuity at the points $\alpha = \pm 90$ deg. The extended function $\hat{F}_y(\alpha)$ is plotted in Fig. 3c.

B. Modeling the Oleos

Oleopneumatic shock absorbers, which use a combination of oil and gas, are used in aircraft because they have the highest energy-dissipation capability for a specific mass ([17], pages 75–77). Single-stage oleos are used for the nose and main landing gears in the model.

We now discuss the design of the spring curve for the oleos. A level attitude is desired when the aircraft is stationary. The static load for the nose and main landing gears is calculated using the maximum aircraft weight at the fore and aft c.g. positions, respectively. The extended/compressed stroke lengths and the stroke required for static loading are set based on the aircraft geometry. The compression ratio between two states of the oleo is the ratio of the respective forces in that state. The following compression ratios are used in the model: 1) static-to-extended ratio of 5:1 and 2) compressed-to-static ratio of 2:1.

The spring curve is fitted to three points: the static load F_s, the extended load F_e, and the compressed load F_c. Figure 4a shows the spring-curve load F_o (kN) against stroke l_s (mm) for the main landing gears.

Figure 4b shows the profile of the damping coefficient C (kg^2/s^2) against stroke l_s for the main landing gears. The dashed curve shows C under extension and the solid curve under compression. The transition between the profile for extension ($V_{oleo} > 0$) and compression ($V_{oleo} < 0$) is continuous because the damping force is proportional to the vertical velocity of the oleo. In the results presented subsequently, the oleos operate with stroke approximately in the range of $l_s \in$ (300–400 mm). The force that the oleo exerts on the airframe is given by

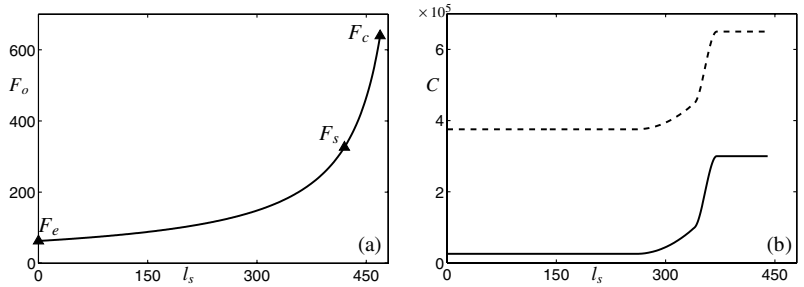

Fig. 4 Oleo characteristics. Panel a shows the spring-curve load F_o (kN) against stroke l_s (mm) for the oleos fitted to three points: the load F_s when the aircraft is statically loaded, the load F_e when the oleo is fully extended, and the load F_c when the oleo is fully compressed. Panel b shows a plot of the damping coefficient C (kg^2/s^2) against stroke l_s (mm) for compression of the oleo (solid curve) and extension of the oleo (dashed curve).

$$F_{\text{oleo}}(l_s) = F_o(l_s) - C(l_s)V_{\text{oleo}} \tag{4}$$

C. Modeling the Aerodynamics

Aerodynamic effects are nonlinear because the forces are proportional to the square of the velocity of the aircraft. The forces also depend nonlinearly on the sideslip angle β and angle of attack σ, due to the geometry of the aircraft. We consider ground maneuvers with no incident wind. Hence, the sideslip angle β is equal to and interchangeable with the slip angle of the aircraft α. Because we are studying ground maneuvers, the angle of attack σ remains relatively steady. There are six components to the aerodynamics forces: three translational forces and three moment forces. The forces and moments on the aircraft are defined in terms of its geometric properties and dimensionless coefficients based on wind-tunnel data and results from computational fluid dynamics. The coefficients used here were obtained from a Group for Aeronautical Research and Technology in Europe (GARTEUR) action group [18] Simulink model in which they are defined using neural networks. Here, the calculation of the longitudinal drag force F_{xA} is explained in detail as an example; each of the other components is determined in a similar fashion. The force F_{xA} is described by the equation

$$F_{xA} = \tfrac{1}{2}\rho|V|^2 S_w C_x \tag{5}$$

where ρ is the density of air, S_w is the wing surface area, $|V|$ is the modulus of the velocity of the aircraft, and C_x is a dimensionless axial force coefficient that depends nonlinearly on the slip angle α and angle of attack σ. Here, C_x is defined over the ranges of $\alpha \in (-10\text{–}10\,\text{deg})$ and $\sigma \in (-2\text{–}5\,\text{deg})$.

While on the ground, the angle of attack σ remains within the range of definition of the GARTEUR data. However, because we wish to consider behavior of the aircraft for slip angles α outside the range of the data, it is necessary to define the functions for all values of $\alpha \in (-180\text{–}180\,\text{deg})$. When looking at behavior for slip angles outside of the range of $\alpha \in (-10\text{–}10\,\text{deg})$, the velocity of the aircraft is sufficiently small ($|V| < 30$ m/s) such that aerodynamic forces are small relative to those generated by the tires. It is sufficient to ensure that the forces are continuous over the full range of α values. The extension of the definition of the axial force coefficients is done in a similar fashion to that of the lateral force functions in Sec. II.A, in which symmetries of the aircraft geometry and saturation values are used.

III. Bifurcation Analysis of Aircraft Turning

In this section, we use continuation software to perform a bifurcation analysis of the preceding aircraft model. We focus on the stability of turning-circle solutions over a range of discrete fixed-thrust levels in which, for each thrust case, the steering angle is varied as a parameter. Each continuation run is executed at a fixed-thrust level that corresponds to a constant straight-line velocity. The aircraft traveling at a constant velocity is a steady-state solution of the system, and these solutions are used as initial points to start individual continuation runs. A proportional–integral thrust controller is used with the steering angle set to 0 deg to obtain the required fixed straight-line velocity. Starting from such an initial solution, the steering angle is varied as a parameter while the stability is monitored. The results from the continuation runs are represented as bifurcation diagrams in which modulus $|V|$ of the velocity of the aircraft is shown. Aircraft trajectory plots are shown with corresponding time histories when appropriate. In the trajectory plots, a trace of the path of the aircraft's c.g. is drawn over the X–Y plane (orthogonal ground-position coordinates). Along the c.g. curve, aircraft markers are drawn at regular time intervals to indicate the attitude of the aircraft relative to the c.g. curve. Note that the attitude of the aircraft on the c.g. curves is equivalent to its slip angle α at that point in the simulation. The markers are not drawn to scale, except when explicitly stated.

A. Low-Thrust Case

Figure 5a shows the continuation curve initiated from an equilibrium state for which the aircraft maintains a constant forward velocity of 70 m/s at 13% of maximum thrust. The resulting solution branch $S1$ of stable (solid) and unstable (dashed) solutions is plotted in the plane of the steering angle δ and the modulus $|V|$ of the aircraft velocity. The stability changes at points H_1 and H_2, which are indicated by stars. On the stable parts of $S1$, the aircraft follows a turning circle, and on the unstable part, more complex stable solutions exist, which are discussed subsequently. Once a steering angle is applied ($\delta > 0$), the tires generate a side force that holds the aircraft in a turning circle. As δ is increased, the velocity of the aircraft rapidly decreases, along with a decrease of the radius of the stable turning circle. The branch becomes unstable at point H_1, where a Hopf bifurcation takes place ([4], pages 248–254). Here, a stable periodic solution is born, as is typical with a Hopf bifurcation. As the steering angle is increased further, the velocity drops less rapidly along the unstable part of the branch, which regains stability at a second Hopf bifurcation H_2. As the steering angle is increased beyond H_2, the aircraft velocity gradually decreases. Along the section of $S1$ between the initial point and H_1, the aircraft follows a large turning circle and all tires' forces remain safely below their saturation levels. Along the section between H_2 and the final point, the aircraft follows a small radius turning circle. As δ increases beyond H_2, the turning circles become tighter, and at $\delta \approx 40$ deg, the outer main gear saturates; effectively, the tire is dragged around the turn. At $\delta \approx 83$ deg, the force generated by the nose gear tire is almost perpendicular to the thrust force and is sufficiently large to hold the aircraft stationary. The aircraft c.g. curve plots in Figs. 5b and 5c correspond to the respective points on $S1$ for $\delta = 3.9$ and 14.9 deg, where the aircraft follows turning circles of radius $r \approx 260$ and 50 m, respectively. Both insets are shown on the same scale and the aircraft markers are also drawn to scale.

We now discuss the behavior of the aircraft for steering angles at which the turning-circle solution is unstable. Figure 6a shows an enlargement of the unstable part of branch $S1$ from Fig. 5a. To find the stable behavior in this region, model simulations are run at discrete values of the steering angle for $\delta \in (4.37\text{–}8.65\,\text{deg})$. After transients have decayed, stable behavior is identified as a branch of periodic solutions. They are represented in Fig. 6a by lines of black dots indicating the minimum and maximum velocities. For a steering angle just below H_2, small oscillations are observed, as is expected just after a Hopf bifurcation. An aircraft c.g. curve and a time plot of aircraft velocity at point c are shown in panels c1 and c2. The trajectory oscillates between turning circles of radius $r_{\max} \approx 90$ m and $r_{\min} \approx 75$ m. Physically, the aircraft approaches its maximum velocity and starts to oversteer. The oversteer increases and the

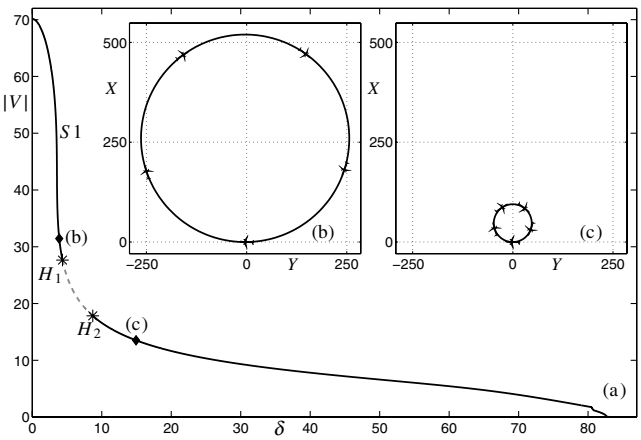

Fig. 5 Panel a is a bifurcation diagram for 13% of maximum thrust with single branch $S1$. Stable parts are solid black lines and the unstable part a dashed gray line. Transitions from stable to unstable branches occur at the Hopf bifurcations H_1 and H_2. Inset panels b and c show the aircraft c.g. curves in the X–Y plane at the respective points on $S1$ for $\delta = 3.9$ and 14.9 deg.

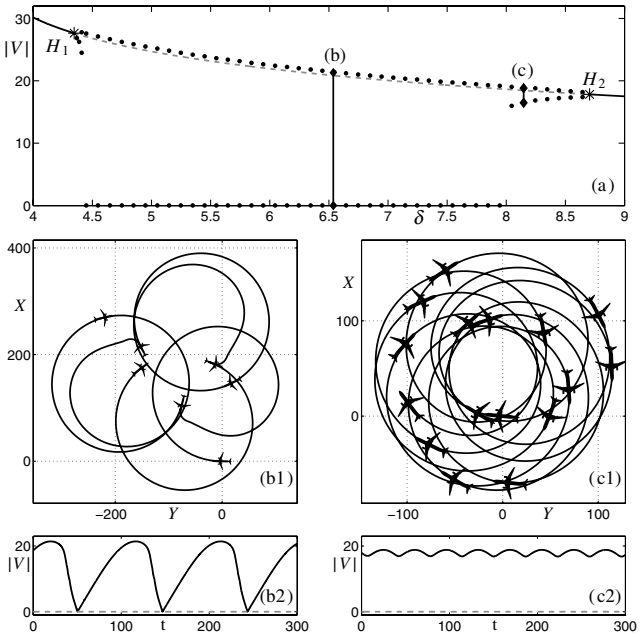

Fig. 6 Panel a shows detail from Fig. 5a with the maximum and minimum aircraft velocity $|V|$ of periodic solutions, shown as black dots, determined by simulations at regularly spaced points between H_1 and H_2. Note the sharp change in the minimum velocity curves at $\delta \approx 4.4$ and 8.0 deg. Panels b1 and c1 show aircraft c.g. curves in the X–Y plane and panels b2 and c2 show time plots of aircraft velocity $|V|$ at points $\delta = 6.54$ (panel b) and 8.14 deg (panel c), respectively.

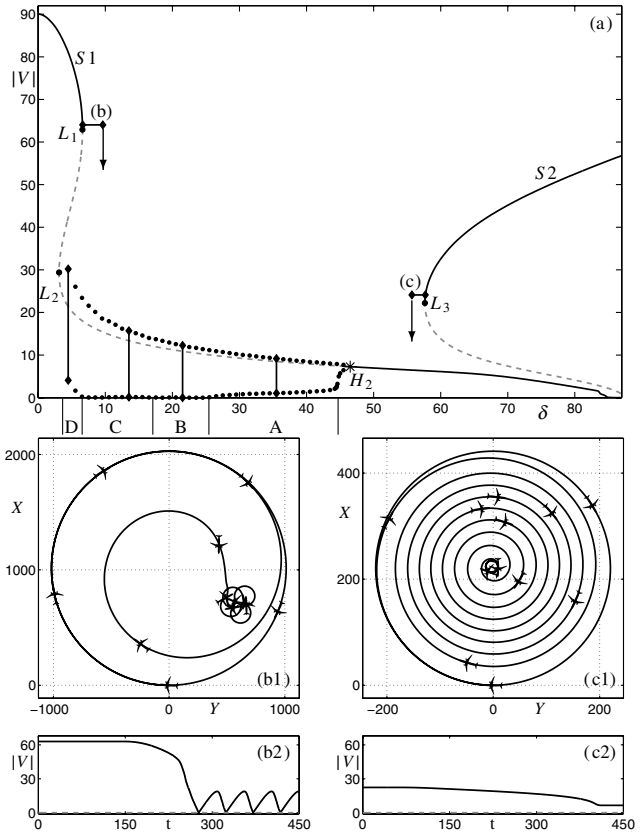

Fig. 7 Panel a shows the bifurcation diagram for 19% of maximum thrust with two disjoint branches $S1$ and $S2$. On $S1$ there are two limit-point bifurcations L_1 and L_2 and a Hopf bifurcation H_2. On $S2$ there is a limit-point bifurcation L_3. Periodic solutions exist along the unstable part of branch $S1$, for which the maximum and minimum velocities are shown by black dots. Four regions A–D, each with a different qualitative behavior, are indicated along the branch. Panels b1 and b2 show an aircraft c.g. curve and velocity plot at point b on $S1$ followed by an increase in steering angle beyond L_1 ($\delta = 6.6$ to 9.6 deg). Similarly, panels c1 and c2 show the transition from point c branch $S2$ to branch $S1$, where the steering angle is decreased past L_3 ($\delta = 57.6$ to 55.6 deg).

velocity drops while the main inner tires saturate and start to skid. The force on the main outer tires increases to compensate, and after a short amount of time, the skid is recovered and the aircraft accelerates again toward its maximum velocity. Note from Fig. 6a that at $\delta \approx 8$ deg there is a sharp increase in the size of these oscillations. It occurs at the point at which the main outer tires saturate after the inner tires and the back of the aircraft skids out. In the region of larger oscillations, the aircraft oscillates between following an approximate turning circle of $r \approx 130$ m and making a 180-deg skid that brings the aircraft to a complete halt. An example c.g. curve and a time plot of aircraft velocity at point b are shown in panels b1 and b2 in Fig. 6. The sharp increase in the size of the oscillations for steering angles just beyond H_1 happens in a similar fashion. Further details of the periodic oscillations are discussed subsequently; their analysis in terms of tire saturation is the focus of Sec. IV.

B. High-Thrust Case

The bifurcation diagram is more complex for a higher-thrust case. Figure 7a shows the curve of steady-state solutions initiated from an equilibrium position at which the aircraft maintains a constant forward velocity of 90 m/s at 19% of maximum thrust. Although this initial velocity is outside the normal operational range for ground maneuvers, the behavior described subsequently does occur at lower velocities: for example, with wet or icy runway conditions. Furthermore, studying solutions outside the normal operational range ensures that all the possible dynamics of the system are identified. The equilibrium branch $S1$ corresponds to that of the lower-thrust case shown in Fig. 5a. The Hopf bifurcation H_2 on branch $S1$ persists. There are two limit-point (or saddle-node) bifurcations L_1 and L_2 that are characterized by a fold in the equilibrium curve and the coexistence of another solution at parameter values before the bifurcation ([4], pages 45–50). Locally, in the case of L_1, a stable and an unstable solution coexist, and in the case of L_2, two unstable solutions coexist. Because of the changes in direction at L_1 and L_2, a hysteresis loop exists for values of δ around these bifurcations. Branch $S1$ is unstable between L_1 and L_2 and between L_2 and H_2. Along the unstable branch of $S1$ between L_2 and H_2 there is a branch of periodic solutions that is discussed subsequently. The maximum and minimum velocities of these solutions are shown as black dots. Furthermore, there is a new branch $S2$ (disjoint from $S1$) with a stable part and an unstable part separated by the limit-point bifurcation L_3.

As is consistent with the lower-thrust case, the aircraft follows a large-radius turning-circle solution on the part of $S1$ between the initial point and L_1. Furthermore, on the stable part of $S1$ beyond H_2, the aircraft follows a tight-turning-circle solution with the outer main gear saturated. Recall that in the case for $\delta > 85$ deg there is a stable solution represented on $S1$ for which the force generated by the nose gear is sufficient to hold the aircraft stationary. In this higher-thrust case, there is the coexisting solution branch $S2$ because the thrust force is sufficient to overcome the holding force generated by the nose gear if the aircraft is in motion. On the stable part of the new branch $S2$, the aircraft follows a large-turning-circle solution with the nose gear saturated.

We now consider the role of the limit-point bifurcations L_1 and L_3. Starting at a solution on the stable part of branch $S1$ and increasing the steering angle just beyond L_1 causes the aircraft to move toward a different attractor. At point b, with the steering angle $\delta = 6.6$ deg, the aircraft follows a turning circle with radius $r \approx 1$ km. When the steering angle is ramped up to $\delta = 9.6$ deg, the aircraft moves toward a different attractor. A c.g. curve plot and velocity $|V|$ time plot are shown in panels b1 and b2 in Fig. 7. In the simulation, the aircraft follows a turning circle until the steering angle is ramped up after 150 s to a value beyond L_1, then the aircraft spirals inward toward a periodic solution similar to that shown in panels b1 and b2 in Fig. 6. There would be no immediate indication to a pilot that the limit-point bifurcation is being approached or passed; the aircraft tends to the

periodic solution over a transient period. Decreasing the steering angle from $\delta = 9.6$ deg (to a value below that at L_2) causes the aircraft to deviate from this periodic solution and return to following a large turning circle on the stable part of branch $S1$. These two transitions between the stable part of $S1$ and the periodic solution existing for values of δ along the unstable part of $S1$ form a hysteresis loop. In the example just described, the aircraft jumps from a stable part of $S1$ to a periodic solution about an unstable part of $S1$. A similar jump, this time between different branches, occurs when starting at a solution on the stable part of branch $S2$ and decreasing the steering angle below L_3. In this case, the aircraft moves from a stable solution on branch $S2$ to a stable solution on branch $S1$. At point c, the steering angle is initially $\delta = 57.6$ deg and ramped down after 70 s to $\delta = 55.7$ deg. Plots of the simulations are shown in panels c1 and c2 in Fig. 7. The aircraft follows a turning circle of radius $r \approx 220$ m and then spirals in toward a turning circle of radius $r \approx 12$ m.

In Fig. 7a, the maximum and minimum velocities of the periodic solutions are shown by dotted black curves. The behavior for a steering angle just below the bifurcation H_2 is shown in panel c1 in Fig. 6. The same behavior persists near H_2 for the higher-thrust case presented in Fig. 7a. As the steering angle is decreased below the bifurcation H_2, the size of oscillations gradually increases. The increase in size of the oscillations corresponds to a greater loss of velocity when the aircraft deviates from the unstable turning-circle solution. Figure 7a shows a steep but apparently smooth increase in the size of oscillations. The steepest part of this increase is at $\delta \approx 45$ deg. For $\delta < 45$ deg, there are much larger oscillations. The transition between the small and large oscillations becomes sharper as lower-thrust cases are considered, as in Fig. 6a. This can be attributed to the fact that the transition from the existence of a stable turning circle for $\delta > H_2$ to the unstable behavior between H_1 and H_2 happens for smaller δ and therefore at a higher velocity in the lower-thrust case. The large oscillations are the subject of Sec. IV.

C. Two-Parameter Bifurcation Diagrams

Having studied the steady-state solutions for two different thrust cases, it is desirable to see whether the behavior persists at different thrust levels. We consider the solutions for constant thrust levels that correspond to discrete initial forward velocities $|V_{\text{init}}| \in (10\text{–}115$ m/s). Figure 8a shows a surface plot of steady-state solutions in (δ, $|V|$, $\%T_{\max}$) space, where $\%T_{\max}$ is the percentage of the maximum thrust of the engines. Figure 8b shows a corresponding contour plot, effectively a top-down view of the surface in the δ–$|V|$ plane. In both plots, the loci of limit-point bifurcations are labeled L and L^*, and the locus of Hopf bifurcations is labelled H. These loci divide the surface: the part above H corresponds to unstable solutions, and the part extending all the way to low values of thrust corresponds to stable solutions. Individual solution branches used to create the surface are shown at regular intervals on the surface by thin black curves. For orientation, the solution branches shown in Figs. 5a and 7a are highlighted by thick black lines on the surface and labeled C_{70} and C_{90}, respectively. In the contour plot, the stability of the contours C_{70} and C_{90} is indicated as in Figs. 5a and 7a.

Bifurcations on the individual solution branches correspond to a crossing of a bifurcation locus curve. The example C_{70} consists of one piece, corresponding to branch $S1$, which intersects the Hopf bifurcation locus curve H in two places, corresponding to the bifurcations H_1 and H_2 in Fig. 5a. The transition between C_{70} and C_{90} is as follows. With increasing thrust levels, two limit-point bifurcations appear at a cusp point on L. The curve H terminates at an intersection with L [a Bogdanov–Takens bifurcation ([19], pages 299–302), not discussed here], and thus the Hopf bifurcation H_1 no longer appears for thrust levels above this intersection. The second branch, $S2$ on C_{90}, can be seen in the background of the surface plot; it is clearly seen in the contour plot in Fig. 8b.

The surface plot reveals that for thrust levels greater than at C_{90}, the structure remains qualitatively the same except that branches $S1$ and $S2$ meet on L^*. For thrust levels below the minimal point on H,

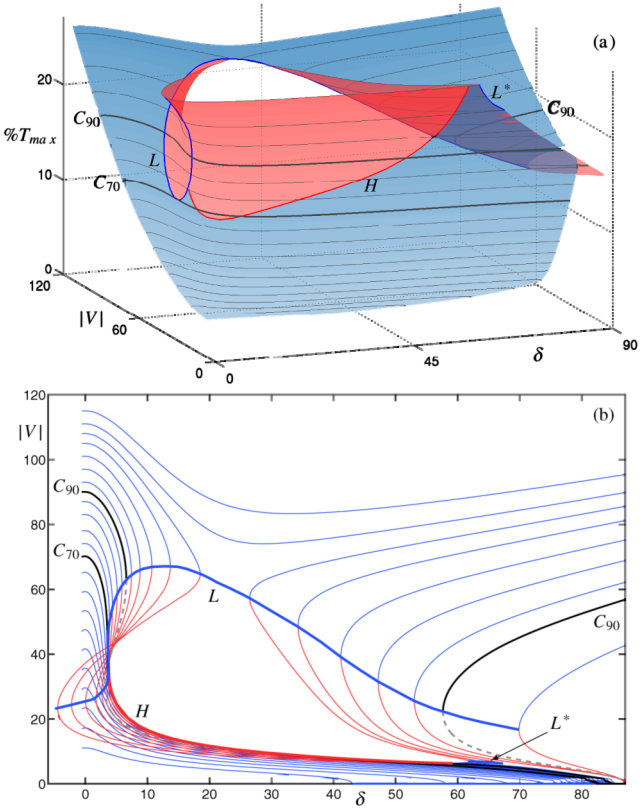

Fig. 8 Panel a shows the surface of turning solutions in ($|V|$, δ, $\%T_{\max}$) space. The loci of limit-point bifurcations L and L^* and the locus of Hopf bifurcations H are indicated by a thick lines; the part of the surface below H and L consists of stable solutions, and the preceding region of unstable solutions. Individual solution branches used to create the surface are shown at regular intervals as thin black curves. The solution branches shown in Figs. 5 and 7 are highlighted by thick black lines and labeled C_{70} and C_{90}, respectively. Panel b shows a corresponding contour plot of individual contours in the $|V|$–δ plane. In the contour plot, the stability of the curves C_{70} and C_{90} has been indicated as in Figs. 5 and 7.

the behavior is trivial; for all values of δ, the solution branches represent stable turning circles. Furthermore, for thrust levels above the saddle point on L, at which point the bifurcations L_1 and L_3 meet and vanish, the behavior is also uniformly stable. Because of the robustness of the structure, the surface in Fig. 8a explains the equilibria dynamics fully. Therefore, by studying the two cases C_{70} and C_{90} in detail and using the surface and contour plots, we have described the underlying dynamics dictating the aircraft's behavior across the entire range of relevant values in the δ–$\%T_{\max}$ plane comprehensively and in a compact manner.

D. Discussions of Bifurcation Results

Bifurcation analysis provides engineers with the underlying dynamic structure that governs the physical behavior that is observed. Changes between qualitatively different types of behavior can be directly attributed to a solution undergoing a bifurcation at a specific parameter value. Of the three nonlinear components in the model, dominant throughout are the tire forces. We found that the oleos do not have a significant effect on the dynamics, but the aerodynamic forces also play an important role at high velocities. The aerodynamic model is based on measured data in the slip-angle range of $\alpha \in (-10\text{–}10$ deg). At lower velocities, which cover a much larger range of slip angles, the aerodynamics forces have a negligible effect. Overall, we can conclude that the aerodynamic model is accurate in the region for which it has a significant effect on the dynamics. Tire force data is only available in a slip-angle range of $\alpha \in (0\text{–}40$ deg). Because the dynamics may cover the entire range of $\alpha \in (-180\text{–}180$ deg) (when the turn is laterally unstable, as discussed in the next section), the tire force needs to be defined for all

values of α. To this end, we extrapolate the lateral tire force so that it continues to drop off as the slip angle increases toward $\alpha = 90$ deg, reaching a minimum of about 30% of its maximum value. Furthermore, the tire force is taken to be symmetrical about the points $\alpha = \pm 90$ deg. The overall tire model is realistic and consistent with the modeling experience at Airbus. Note that for the fixed turning solutions we found in the bifurcation study, the slip angle never exceeds $\alpha = 90$ deg.

As an example of how bifurcation analysis can uncover even quite subtle effects of practical interest, we consider the dynamics near the upper-left limit point in Fig. 7a. A small change in the steering angle leads to the loss of lateral stability, but it is not immediately obvious how to relate this observation to inherent properties of the aircraft system that could be monitored. Further investigation indicates that the loss of stability is due to the diminishing influence of the aerodynamic forces due to the rapid loss of velocity as the limit point is approached. Namely, at low velocities, an aircraft tends to oversteer, whereas at high velocities, it understeers because the aerodynamic forces try to keep the aircraft in a straight line. Passing the limit point appears to correspond to the transition from understeer maintained by large aerodynamic forces to a low-velocity oversteer solution, with the result that the aircraft attempts to follow a tighter turning circle. This observation shows that bifurcation analysis can reveal features of the dynamics that otherwise would not be immediately evident. Another example is the determination of the maximum lateral load. The present lateral ground load regulation of 0.5 g is known to be very conservative, and recent studies by the Federal Aviation Administration have shown that large transport aircraft seem to have an upper limit of approximately 0.35 g [20]. Nonlinear effects make it difficult to determine where the maximum lateral load will occur by standard techniques. It is proposed that the boundaries of the bifurcation diagrams may indicate where this maximum lateral loading condition may occur, and this will form part of our future work.

IV. Different Types of Periodic Solution

We now study the branch of periodic solutions in Fig. 7a for $\delta \in (4.5\text{–}46.5$ deg) in more detail. An attempt was made to follow the periodic solutions using AUTO, but it was only possible to find very short branches near the Hopf bifurcations. Because of the black-box nature of the SimMechanics model, it is difficult to assess the reason for this computational difficulty, but it may be related to the rapid growth of the solution profile. As an alternative, we found the periodic solutions by simulation runs for discrete values of the steering angle. The stable periodic behavior was found by running the model from an initial state of the system on the stable part of branch $S1$ near the bifurcation H_2 and ramping down the steering angle. Once any transient behavior has passed, the persistent behavior is studied. The region of larger oscillations (for $\delta < 45$ deg) can be divided into four subintervals that correspond to different types of periodic solution. Specifically, we distinguish type A, $\delta \in (25.5\text{–}44.5$ deg); type B, $\delta \in (17.5\text{–}25$ deg); type C, $\delta \in (7\text{–}17$ deg); and type D $\delta \in (4.5\text{–}6.5$ deg).

The boundary between regions A and B is the point at which the minimum velocity of the periodic solution first reaches $|V| = 0$. Similarly, the transition from regions C to D is associated with the minimum velocity becoming nonzero again.

Figure 9 shows c.g. curves plotted in the X–Y plane over one period of motion, with corresponding time-history plots of the aircraft velocity $|V|$ and the slip angle α. Plotted is the stable behavior at δ values that are representative of the four intervals A–D shown in Fig. 7. Across each region, the behavior is qualitatively the same. The aircraft slip angle gives the aircraft's orientation relative to its direction of motion. Recall that the slip angle is used to calculate the orientation of the markers on the c.g. curves. For each of the types A–D, there are common features that can be identified. The data is plotted over one period taken between points of maximum velocity. Therefore, the initial points represent the aircraft approximately following the unstable turning circle but at a slightly higher velocity. The turning-circle solution is unstable and so the aircraft deviates

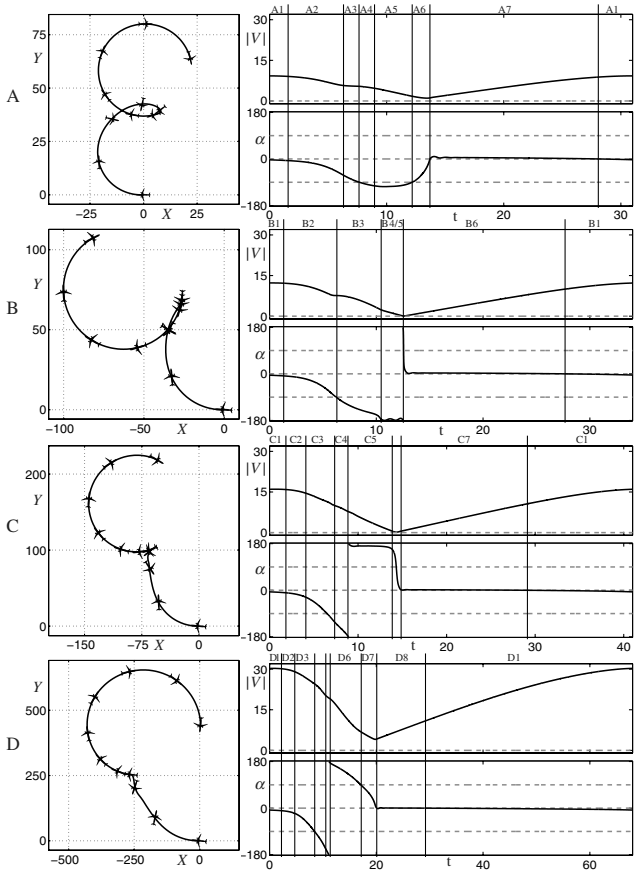

Fig. 9 Panels on the left show aircraft trajectories exhibiting the qualitatively different periodic behavior in the regions A–D shown in Fig. 7a. Panels on the right are the corresponding plots of the aircraft velocity $|V|$ and aircraft slip angle α against time t for each case. In the time plots, the lines $|V| = 0$, $\alpha = 0$, and $\alpha = \pm 90$ are represented by dashed gray lines. These time-history plots are divided into time intervals that correspond with the changing aircraft states described in Figs. 10–13.

from it, loses velocity, and comes to a near or full stop. The point of minimum velocity corresponds to the point of maximum curvature on the aircraft c.g. curve. Because of the constant thrust, the aircraft then speeds up once more, approaching the turning circle before again reaching the maximum velocity at the final point. From the plots in the left column, a longer trajectory is obtained by repeatedly copying and translating each trajectory so that the start and final points connect. Panel c1 in Fig. 6 is an example of what such a trajectory looks like.

The time plots in the right column of Fig. 9 are divided into numbered time intervals, each representing a qualitative state of the aircraft. Transitions between the intervals indicate a qualitative change. For example, for type A, the transition between steps A3 and A4 corresponds to the modulus of the aircraft slip angle $|\alpha|$ exceeding 90 deg. This means that the aircraft has rotated beyond slipping sideways relative to its direction of motion and has a backward component to its motion. Clearly, it is necessary to look at other features of the aircraft behavior to fully explain all these transitions. Therefore, we now introduce a diagrammatic representation that takes into account many aspects of the aircraft's behavior, to give a very detailed account in each case.

The overall behavior in regions A–D is as follows: In type A, when the aircraft deviates from the unstable turning-circle solution, it enters a skid and loses velocity until the skid is recovered and the aircraft starts to approach the unstable turning-circle solution again as it speeds up. In type B, the aircraft enters a skid in a similar fashion to type A but skids around almost 180 deg and rolls backward before coming to a complete stop. Type C is similar to type B, but now the aircraft skids through 180 deg and briefly follows a backward turning

circle before stopping. In types B and C, the skid is only recovered when the aircraft comes to a halt. After stopping, it speeds up again and approaches the unstable turning-circle solution. In type D, the aircraft enters a skid and makes a full rotation relative to its c.g. curve without coming to a stop. The skid is only recovered when the aircraft is traveling forward again.

A. Diagrammatic Representation

Figures 10–13 each show time plots of the nose tire slip angle α_N and main outer tire slip angle α_M for types A–D. We do not distinguish between the behavior of the inner and outer main gears because both gears act practically simultaneously in the cases studied. The tire forces are larger on the outer gear due to a greater load. Therefore, the slip angle of the outer gear α_M is used to represent the behavior of both the main gears. In the time-history plots of Figs. 10–13, there is a dashed black line indicating the optimal slip angle at which the tire will generate the greatest holding force. These plots show concurrent information with the plots in Fig. 9. The plots are divided into numbered regions for which a given aircraft state can be identified.

For each of the numbered regions in the time plots of Figs. 10–13, there is a corresponding diagram at the top of the figure. Each diagram shows several pieces of information about the state of the aircraft. Recall that the aircraft markers in the c.g. curve plots of Fig. 9 indicate the slip angle of the aircraft: that is, the angle it makes with its direction of motion. The direction of motion is indicated in the diagrams in Figs. 10–13 by an arrow originating from the c.g. position that is pointing to the left. The slip angle of the aircraft in the diagrams is indicated schematically as one of the values $\alpha = \pm 10$, ± 45, ± 135, or ± 170 deg. The direction of rotation of the aircraft, taken from the sign of the rotational velocity of the aircraft, relative to the c.g. curve is shown about a representative center of rotation; it may be in front of the nose gear, between the nose and main gears, or behind the main gears. The (approximate) location of the three landing gears is represented by two black tires (the nose and outer main gear) and a gray tire (the inner main gear). Recall that we consider the main gears to act simultaneously and therefore only represent the behavior at the outer gear. The directions of tire forces are shown on the nose gear and main outer gear. From each of the nose and main outer gears originates a double arrow indicating the direction of the tire force as determined by the sign of the tire slip angles $\alpha_{N,M}$. Passing through the lines $\alpha_{N,M} = 0$ or ± 180 deg indicates that the direction of the tire force changes. The size of these arrows is uniform and does not indicate the magnitude of the forces. Finally, a single arrow is shown opposing the tire force direction if that particular tire is skidding. In general, when the tires are rolling and generating a holding force sufficient to control the aircraft, the slip angles will change gradually. A tire is identified as skidding if the slip angle crosses through the optimal holding force line and the slip angle starts to change rapidly. A tire is identified as having recovered from skidding when the time derivative of its slip angle returns toward 0 (the slip-angle curve plateaus out).

B. Detailed Discussion of Types A–D

We now discuss the aircraft dynamics for types A–D. After a brief summary, each periodic state of the aircraft is explained in detail. The reader will find it useful to refer back to Fig. 9.

1. *Type A*

As shown in Fig. 10, $\delta \in (25.5\text{–}44.5$ deg). The aircraft is initially at the maximum velocity and has started to deviate from the unstable turning-circle solution; the velocity then drops as the main tires start skidding. The aircraft continues to slow down. The skid is recovered when the aircraft reaches its minimum velocity. The aircraft approximately follows a turning circle as it speeds up from the minimum velocity.

In step A1, the aircraft approximately follows the unstable turning-circle solution, held by tire forces; that is, it rotates clockwise about a point in front of the nose gear, and the aircraft slip angle α is small. The aircraft slip angle α increases as the aircraft gains velocity and gradually starts to oversteer.

In step A2, the main tires saturate (in quick succession, inner followed by outer) and start to skid. The main tire slip angle α_M passes through the optimal slip-angle line, after which its slope increases rapidly. The aircraft begins to oversteer excessively and the aircraft slip angle α changes rapidly; the rotational velocity of the aircraft increases.

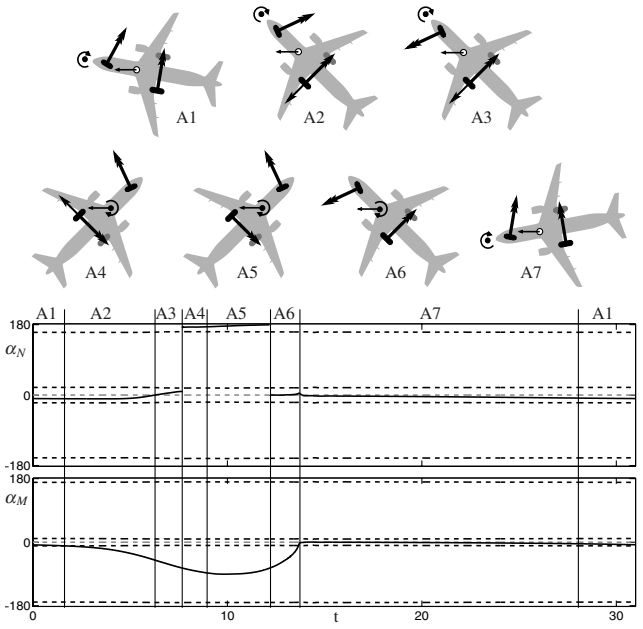

Fig. 10 Diagrammatic representation of the periodic behavior of the aircraft for region A in Fig. 7. The two panels show the nose tire slip angle α_N and main tire slip angle α_M over one period (black curves). The optimal slip-angle values are shown by dashed black lines. The line $\alpha_{N,M} = 0$ is shown as a dashed gray line. Each aircraft diagram represents the aircraft's state over the numbered time intervals on the time-history panels.

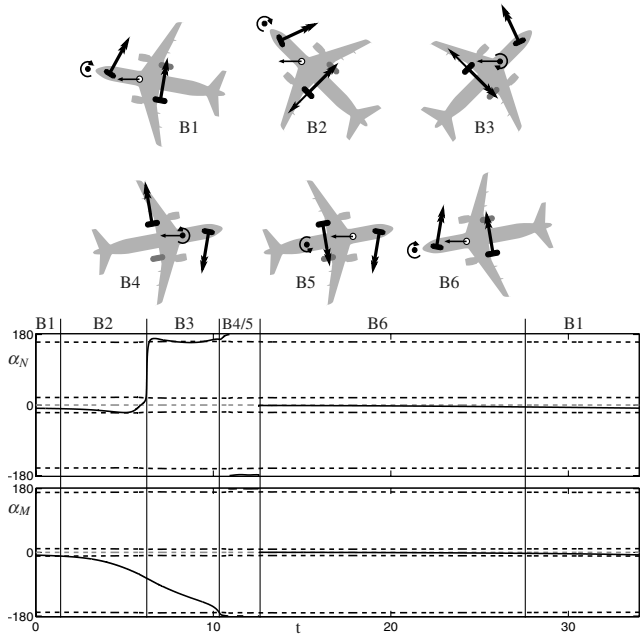

Fig. 11 Diagrammatic representation of the periodic behavior of the aircraft for region B in Fig. 7. The two panels show the nose tire slip angle α_N and main tire slip angle α_M over one period (black curves). The optimal slip-angle values are shown by dashed black lines. The line $\alpha_{N,M} = 0$ is shown as a dashed gray line. Each aircraft diagram represents the plane's state over the numbered time intervals on the time-history panels.

In step A3, the main gears continue to skid. The force on the nose gear switches (α_N changes sign) to oppose the rotation of the aircraft causing the rotational velocity to fall.

Step A4 is the same as step A3 but the slip angle exceeds $|\alpha| > 90$ deg (see Fig. 9); the aircraft moves beyond sliding sideways with a slight backward component to the motion. The center of rotation of the aircraft moves through the nose gear causing a sudden jump in its slip angle α_N.

In step A5, the main tires regain traction, evidenced by the main tire slip angle α_M plateauing out, and so both the nose tires and main tires oppose the spin, effectively bringing the spin under control. The slip angle of the aircraft α plateaus out as it regains control.

In step A6, the aircraft has stopped skidding and starts to travel forward again; the slip angle has fallen below $|\alpha| = 90$ deg and therefore there is no backward component to its motion. It continues to slow down toward its minimum velocity. Although the main tire slip angle α_M changes rapidly, the tire force is increasing. This is because the slip angle does not pass through an optimal slip-angle line.

In step A7, when the aircraft reaches its minimum velocity, the sign of α_N changes so that the direction of the nose tire force matches the main gears. The aircraft speeds up and starts to follow an approximate turning circle. Initially, while traveling at low velocity, the aircraft understeers slightly before starting to oversteer at the transition back into step A1.

Note that for $\delta \in (40.5\text{–}44.5$ deg) in type A, the aircraft slip angle does not exceed $|\alpha| > 90$ deg, and in this case, steps A4 and A5 do not occur in Fig. 10.

2. *Type B*

As shown in Fig. 11, $\delta \in (17.5\text{–}25$ deg). The aircraft enters a skid in a similar way to type A but does not recover from the skid. The aircraft skids around almost 180 deg and only stops skidding when the tires are rolling backward. The aircraft rolls backward, oscillating from side to side with a slip angle just greater than $\alpha = -180$ deg. The constant forward thrust brings the aircraft to a halt; the slip angle α passes through $\alpha = -180$ deg to become positive and returns rapidly toward $\alpha \approx 0$ deg as the aircraft starts moving forward again. The significant difference with type A is that the aircraft makes a full rotation relative to the c.g. curve and also that the aircraft comes to a complete halt ($|V| = 0$). After coming to a halt, it starts to move off again following an approximate turning circle.

Step B1 is the same as step A1.

Step B2 is the same as step A2.

In step B3, the direction of the force on the nose gear changes as the aircraft starts to rotate about a point between the nose and main gears. Simultaneously, the slip angle exceeds $|\alpha| > 90$ deg, qualitatively the same as step A4, effectively missing out step A3 because the aircraft rotates faster in the skid.

In steps B4 and B5, the aircraft skids around far enough such that the tires regain traction while rolling backward. The aircraft slip angle α plateaus out into a region of small oscillations just above $\alpha = -180$ deg. As the aircraft travels backward, the momentum from the skid causes it to roll from side to side (the wing tips move up and down). The forces on the main tires switch from side to side and the direction of rotation alternates, switching between steps B4 and B5. As the aircraft is traveling backward, the constant thrust rapidly slows it down, bringing it to a complete halt. The slip angle passes through $\alpha = -180$ deg, becoming positive and rapidly returning toward $\alpha = 0$ deg.

In step B6, the aircraft moves off from stationary following an approximate turning circle, the same as step A7.

3. *Type C*

As shown in Fig. 12, $\delta \in (7\text{–}17$ deg). The aircraft enters a skid in a similar fashion to types A and B, but it skids over 180 deg before the tires stop skidding. The aircraft briefly follows a backward turning circle while the forward thrust slows it down. Although the translational velocity reaches $|V| = 0$, it still has rotational velocity at that point. The significant difference from type B is that the aircraft tires regain traction after it has spun over 180 deg (i.e., the slip angle has passed through $\alpha = -180$ deg). The momentum from the skid maintains a rotational velocity when the aircraft travels backward. After stopping (translationally, not rotationally) the aircraft then moves off following a turning circle in the forward direction.

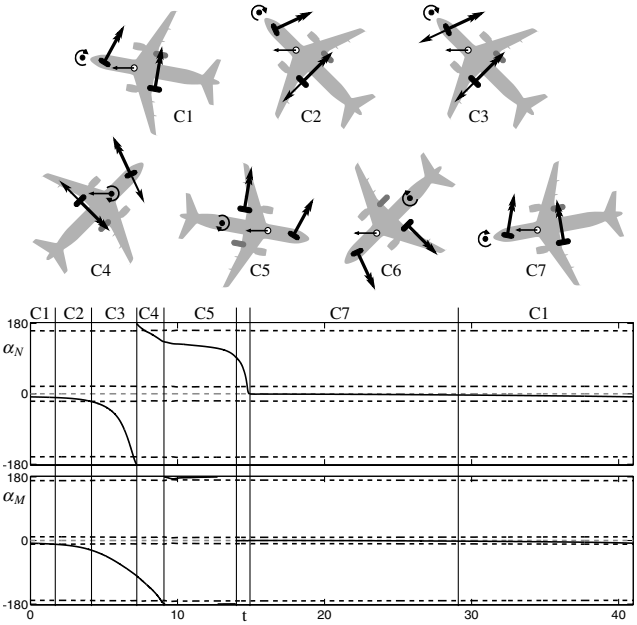

Fig. 12 Diagrammatic representation of the periodic behavior of the aircraft for region C in Fig. 7. The two panels show nose tire slip angle α_N and main tire slip angle α_M over one period (black curves). The optimal slip-angle values are shown by dashed black lines. The line $\alpha_{N,M} = 0$ is shown as a dashed gray line. Each aircraft diagram represents the plane's state over the numbered time intervals on the time-history panels.

Step C1 is the same as steps A1 and B1.

Step C2 is the same as steps A2 and B2.

In step C3, the aircraft has more momentum because, in this case, the velocity is higher when the aircraft enters a skid. Traction on the main and nose tires is lost before the aircraft slides past $\alpha = 90$ deg. In contrast to the previous cases, all tires are skidding. The slope of the aircraft slip angle α increases.

In step C4, the direction of the force on the nose tire switches and the center of rotation moves to a position between the main and nose gears. All the tires oppose the direction of rotation but are skidding. The aircraft slip angle α continues to changes rapidly.

In step C5, the aircraft slip angle moves through $\alpha = -180$ deg, after which the main tires and the nose tires regain traction. The aircraft follows a backward turning circle with a small, almost constant, aircraft slip angle α. The main tire slip angle α_M remains very small and does change sign once (although this is not indicated in the diagram).

In step C6, the aircraft (translational) velocity reaches $|V| = 0$ instantaneously, but as it passes through this point, it still has rotational velocity. The momentum of the aircraft causes it to carry on rotating in the same direction as it travels backward. The aircraft starts to accelerate again, moving in a forward direction, due to the constant thrust.

Step C7 is the same as steps A7 and B6.

4. *Type D*

As shown in Fig. 13, $\delta \in (4.5\text{–}6.5$ deg). The aircraft enters a skid at a higher velocity than in the previous cases. The aircraft has more momentum, so that it makes a full 360-deg spin relative to the c.g. curve before traction on the tires is regained. In contrast to the previous two cases, when the aircraft travels backward, the tires continue skidding. Once the aircraft is facing forward after the spin, it has lost sufficient momentum for the tires to stop skidding and the aircraft returns to following an approximate turning circle.

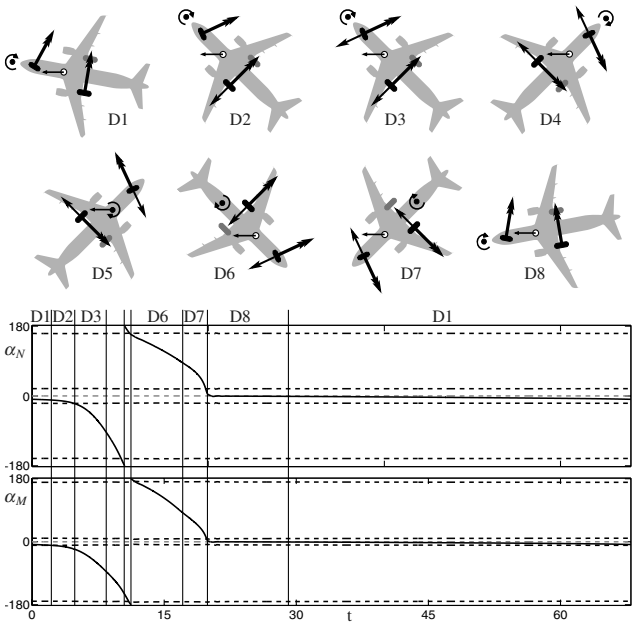

Fig. 13 Diagrammatic representation of the periodic behavior of the aircraft for region D in Fig. 7. The two panels show the nose tire slip angle α_N and main tire slip angle α_M over one period (black curves). The optimal slip-angle values are shown by dashed black lines. The line $\alpha_{N,M} = 0$ is shown as a dashed gray line. Each aircraft diagram represents the plane's state over the numbered time intervals on the time-history panels.

Step D1 is the same as steps A1, B1, and C1.

Step D2 is the same as steps A2, B2, and C2.

Step D3 is the same as step C3.

In step D4, the aircraft continues to skid, the slip angle exceeding $\alpha = 90$ deg before direction of the force on the nose gear changes. The center of rotation stays at a point in front of the nose gear.

Step D5 is the same as step C4.

In step D6, the aircraft spins through $\alpha = 180$ deg, the tires not regaining traction. The force on the main tires changes direction and the aircraft now spins about a point behind the main gears.

In step D7, the aircraft continues to rotate and return toward facing forward while slowing to a low velocity.

In step D8, as the aircraft returns to traveling in a forward direction ($\alpha \approx 0$), the tires regain traction and the aircraft speeds up following a turning circle (the same as steps A7, B6, and C7).

Types A–D provide a complete explanation of the behavior when lateral stability of the aircraft is lost. From case to case, the velocity at which lateral stability is lost increases. Therefore, more momentum is available so that aircraft undergoes a larger rotation before the tires regain traction. The level of detail shown in our new diagrammatic representation is necessary to fully explain the different types of periodic behavior and the transitions between them.

V. Conclusions

A bifurcation analysis of the turning maneuvers of an Airbus A320 on the ground was presented. Focusing on a particular aircraft configuration, the stability of turning-circle solutions was computed over the entire range of relevant values of steering angle and thrust. It is the stability of these turning-circle solutions that dictates whether a particular turning maneuver at specific parameter values is laterally stable. The results were rendered as a surface plot, which was constructed from continuation runs with varying steering angle δ at discrete fixed-thrust levels. The modulus of the velocity of the aircraft $|V|$ was used in this representation, meaning that the surface is represented in (δ, $|V|$, $\%T_{\max}$) space. We found that the single parameter continuation curves corresponding to fixed-thrust levels are qualitatively the same over large ranges of thrust. Because of this robustness in the structure of the surface, it was possible to fully explain the dynamics represented on the surface by studying two individual thrust cases in detail. These two cases were explained in terms of the solutions represented by the bifurcation diagrams. Examples were given of branch switching near limit-point bifurcations and the periodic solutions that arise from Hopf bifurcations. In this way, two significant types of behavior were identified: stable turning-circle solutions and periodic solutions for which the aircraft loses lateral stability when entering a skid or even a spin.

In conjunction with the bifurcation analysis, model simulations were used to study periodic orbits in the region of unstable turning solutions. A detailed explanation of the dynamics was given by means of a diagrammatic representation of changing states of the aircraft. The focus was on attributing qualitative changes in the behavior under parameter variation to the saturation of the forces generated by individual tires. Four regions of qualitatively different behavior were identified, and the differences and transitions between them were explained. The diagrammatic explanation gave details of the undesirable behavior when the aircraft loses lateral stability. The safe operating limits, avoiding this behavior, were identified over the relevant ranges of steering angle and thrust by the bifurcation analysis. Specifically, our results identify that for high-velocity turns, such as when exiting the runway, maintaining a steering angle below $\delta = 4$ deg ensures lateral stability. Furthermore, a curve of Hopf bifurcations in the steering angle versus thrust parameter space is identified as the boundary for lateral stability when performing high-steering-angle maneuvers at lower velocities.

Acknowledgment

This research is supported by an Engineering and Physical Sciences Research Council (EPSRC) Case Award grant in collaboration with Airbus in the United Kingdom.

References

[1] Klyde, D. H., Myers, T. T., Magdaleno, R. E., and Reinsberg, J. G., "Identification of the Dominant Ground Handling Characteristics of a Navy Jet Trainer," *Journal of Guidance, Control, and Dynamics*, Vol. 25, May 2002, pp. 546–552; also AIAA Paper 2000-3903, 2000.

[2] Klyde, D., Myers, T., Magdaleno, R., and Reinsberg, J., "Development and Evaluation of Aircraft Ground Handling Maneuvers and Metrics," AIAA Atmospheric Flight Mechanics Conference, AIAA, Paper 2001-4011, 2001.

[3] Klyde, D. H., Magdaleno, R. E., and Reinsberg, J. G., "The Effect of Tire Pressure on Aircraft Ground Handling," *Journal of Guidance, Control, and Dynamics*, Vol. 26, July 2003, pp. 558–564; also AIAA Paper 2002-4798, 2002.

[4] Strogatz, S., *Nonlinear Dynamics and Chaos*, Springer, New York, 2000.

[5] Guckenheimer, J., and Holmes, P., *Nonlinear Oscillations, Dynamical Systems and Bifurcations of Vector Fields, Applied Mathematical Sciences*, Vol. 42, Springer, New York, 1983.

[6] AUTO, Software Package, Ver. 97, Concordia Univ., Montreal, 1997.

[7] Krauskopf, B., Osinga, H. M., and Galán-Vioque, J., *Numerical Continuation Methods for Dynamical Systems*, Springer, New York, 2007.

[8] Thompson, J. M. T., and Macmillen, F. B. J. (eds.), "Nonlinear Flight Dynamics of High-Performance Aircraft," *Philosophical Transactions of the Royal Society of London, Series A: Mathematical and Physical Sciences*, Vol. 356, No. 1745, Oct. 1998, pp. 2167–2180. doi:10.1098/rsta.1998.0268

[9] Venn, D., and Lowenberg, M., "Non-Linear Vehicle Dynamics Using Bifurcation Methods," Motorsports Engineering Conference and Exhibition, Society of Automotive Engineers Paper 2004-01-35332004.

[10] SimMechanics, Software Package, Ver. 2.7.1, The MathWorks, Inc., Natick, MA, 2004.

[11] Blundell, M., and Harty, D., *The Multibody Systems Approach to Vehicle Dynamics*, Society of Automotive Engineers, Warrendale, PA, Sept. 2004.

[12] Coetzee, E., "Nonlinear Aircraft Ground Dynamics," M.Sc. Thesis, Univ. of Bristol, Bristol, England, U.K., 2006.

[13] Khapane, D. P., "Simulation of Asymmetric Landing and Typical

Ground Maneuvers for Large Transport Aircraft," *Aerospace Science and Technology*, Vol. 7, No. 8, 2003, pp. 611–619. doi:10.1016/S1270-9638(03)00066-X

[14] Allgower, E. L., and Georg, K., *Introduction to Numerical Continuation Methods*, Society for Industrial and Applied Mathematics, Philadelphia, Dec. 2003.

[15] Wong, J., *Theory of Ground Vehicles*, 3rd ed., Wiley-Interscience, New York, Mar. 2001.

[16] Mitchell, D., "Calculation of Ground Performance in Take-Off and Landing," Engineering Sciences Data Unit, Data Sheet ESDU 85029, London, 1985.

[17] Currey, N., *Aircraft Landing Gear Design: Principles and Practices*, AIAA, Washington, D.C., 1988.

[18] Jeanneau, M., "Description of Aircraft Ground Dynamics," Group for Aeronautical Research and Technology in Europe, Rept. FM AG17 RP0412731, 2004.

[19] Kuznetsov, Y., *Elements of Applied Bifurcation Theory*, Applied Mathematical Sciences, Vol. 112, Springer–Verlag, New York, Sept. 1998.

[20] Tipps, D., Rustenburg, J., Skinn, D., and DeFiore, T., "Side Load Factor Statistics From Commercial Aircraft Ground Operations," Univ. of Dayton TR 2002-00119, Dayton, OH, Jan. 2003.